ADVANCED MATERIALS INTERFACES
Open Access
www.advmatinterfaces.de

Plasmonic Resonance Shifts in Gold Nanoparticles-Thermochromic VO_2 Thin Film Hybrid Platforms: A Joint Experimental and Numerical Study

Grégory Savorianakis, Cédric Rousseau, Anastasiya Sergievskaya, Gilles Rosolen, Michel Voué, Bjorn Maes, and S. Konstantinidis**

The combination of the phase transition in thermochromic vanadium dioxide (VO_2) with plasmonic nanoparticles paves the way for applications in various fields, including optical sensing, advanced coatings, and dynamic optical devices. This study presents a simple fabrication method to control both the size and surface coverage of NPs combined with VO_2. First, a thermochromic VO_2 coating with a phase transition at 68 °C is synthesized using reactive magnetron sputtering. Then, monodisperse 30 nm diameter gold NPs are bonded to the VO_2 surface using (3-aminopropyl)trimethoxysilane (APTMS) linkers, examining the effect of immersion duration on surface coverage. Two platforms are developed: a VO_2 thin film with a monolayer of NPs and a configuration with NPs between two VO_2 films. The temperature-dependent plasmonic response of these platforms is measured by extinction spectroscopy, showing a significant wavelength resonance shift of approximately 10 nm for the first platform and 20 nm for the second. Optical simulations analyze this shift over various geometries, from isolated NPs to fully covered NPs, achieving a 60 nm shift for NPs embedded in a thin VO_2 film. This study demonstrates an effective approach to synthesizing thermochromic VO_2 coatings with gold NPs, offering insights into the plasmonic properties of hybrid platforms.

1. Introduction

Since the pioneering work of F. J. Morin[1] vanadium dioxide (VO_2) has garnered significant attention due to its rapid and reversible first-order semiconductor-to-metal transition, occurring at 68 °C. The transition from a monoclinic semiconductor phase to a rutile metallic one results in an important modification in optical and electrical characteristics. For these reasons, monoclinic VO_2 is hence referred to be thermochromic. These particular properties make it a great option for studying transition mechanisms and exploring its potential applications in photonic devices,[2] tunable optical filters,[3] and energy-saving windows.[4,5] Various techniques can be employed to synthesize VO_2 thin films, including sol–gel,[6] thermal evaporation,[7] pulsed laser deposition,[8,9] and magnetron sputtering,[10] the latter being the method employed in this study. These synthesis techniques allow for the precise fabrication of VO_2 films, and for the control of the interfaces, enabling further investigation of their properties and potential integration into a wide range of applications. Moreover, VO_2 can also be synthesized under a nanoparticles form.[11,12]

In recent years, several studies focused on exploring the plasmonic behavior of thermochromic VO_2 in combination with metal nanoparticles (NPs). Noble metal NPs, such as Ag, Au,

G. Savorianakis, A. Sergievskaya, S. Konstantinidis
Plasma-Surface Interaction Chemistry (ChIPS)
Research Institute for Materials Science and Engineering
University of Mons
20 Place du Parc, Mons B-7000, Belgium
E-mail: gregory.savorianakis@umons.ac.be;
stephanos.konstantinidis@umons.ac.be

The ORCID identification number(s) for the author(s) of this article can be found under https://doi.org/10.1002/admi.202400172

DOI: 10.1002/admi.202400172

G. Savorianakis, M. Voué
Physics of Materials and Optics Group (LPMO)
Research Institute for Materials Science and Engineering
University of Mons
20 Place du Parc, Mons B-7000, Belgium

C. Rousseau, G. Rosolen, B. Maes
Micro- and Nanophotonic Materials Group (MMNP)
Research Institute for Materials Science and Engineering
University of Mons
20 Place du Parc, Mons B-7000, Belgium

and Cu, exhibit distinctive optical spectra characterized by an absorption band in the visible region,[13] which does not occur in bulk metal. This absorption is caused by a localized surface plasmon resonance (LSPR), which is described by an oscillation of conduction electrons in response to light excitation. Excitation of the LSPR leads to wavelength-selective photon absorption, light scattering, and amplification of the electromagnetic field. These properties render metallic NPs particularly useful in a wide range of technical applications, including optical devices, plasmonics, sensors,[14] Raman scattering spectroscopy[15] and so on. The LSPR band characteristics are highly sensitive to factors such as NP size, shape, coverage density, and refractive index of the surrounding environment.[16] Any alteration in these factors results in optical phenomena, including as main effect a shift in the peak absorption wavelength (λ_{LSPR}). The modulation of the NP plasmon resonance wavelength could therefore be induced by the temperature-dependent modification of the VO_2 refractive index if such hybrid materials are successfully synthesized.

In consequence, heterostructures composed of metallic NPs, such as Au and Ag, embedded within or surrounded by VO_2, have recently attracted interest due to the enhanced tunability of the λ_{LSPR}.[17,18] Tunable plasmonic resonances have been investigated in VO_2-Ag nanocomposites, where the plasmon wavelengths exhibit a blue shift with increasing temperature. Additionally, studies have explored devices incorporating Au nanoparticles on top of VO_2 thin films, further demonstrating the potential for tuning plasmonic properties in these systems.[15,18] The authors of the latter paper use a sputtering technique to deposit NPs on VO_2. With that technique, important parameters such as the NP size and their surface coverage are not individually manageable, including the shape of the NPs, which usually diverges from a sphere. The present study proposes a way to create similar platforms, while offering the opportunity to monitor these key parameters independently.

Herein, we investigate the LSPR of Au NPs bound to a surface of thermochromic VO_2 utilizing organic linkers with length less than 1 nm.[19] The conditions for coupling VO_2 and Au NPs are provided. Subsequently, we evaluate how temperature variation affects the LSPR resonance wavelength in two experimental cases: NPs on top of a VO_2 film (NPs/VO_2), and NPs embedded in VO_2 (VO_2/NPs/VO_2, 'sandwich' structure). Then, by making extensive use of optical modeling techniques, we examine a large range of geometries, both the experimental ones and other cases with different overlayer thicknesses, giving us a detailed view of the plasmon shift as a function of VO_2 coverage. It turns out that the highly localized electromagnetic field is very rapidly sampled by a minute VO_2 overlayer, offering very strong shifts as a function of its thickness.

The paper is structured as follows. Section 6 introduces the experimental methods in terms of VO_2 thin film synthesis, characterization, NP synthesis, and functionalization and the simulation tool used. Section 2 is devoted to characterization of the thermochromic thin films, whereas Section 3 concerns the optical temperature-dependent response on the different platforms NPs/VO_2 and VO_2/NP/VO_2. The last section (Section 4) provides simulation results for a sequence of configurations corresponding to different NP incorporations into VO_2. Starting from NPs in air and finishing with NPs entirely embedded in the

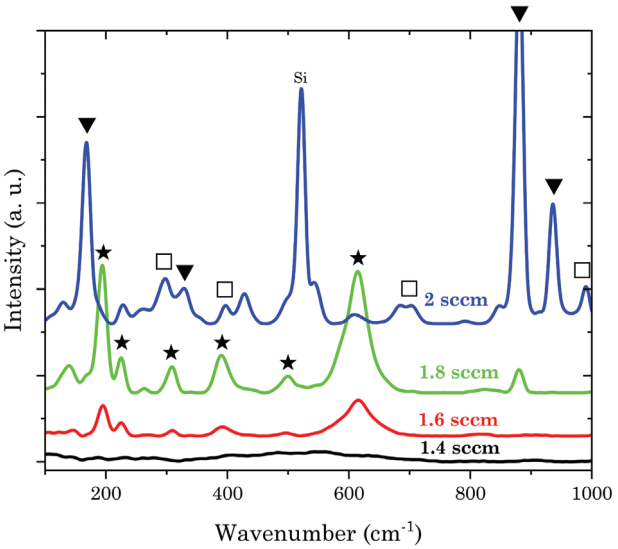

Figure 1. Raman spectra of the 200 nm vanadium oxide thin films according to the oxygen flow during the deposit. The thermal annealing is carried out at 500 °C during 2h for all samples (stars: VO_2,[21] triangles: V_7O_16,[22] squares: V_2O_5).[23] All samples are deposited on Si and the Si peak appears at 520 cm^{-1}.

VO_2 matrix, the plasmonic peak position and the shift between the 'cold' and 'hot' state is calculated. Conclusions are provided in Section 5.

2. Thermochromic Thin Film Characterization

In this section, the crystalline composition and phases within the film are determined by Raman spectroscopy. Subsequently, transmission and reflection measurements at 25°C (referred as 'cold' state) and 100°C ('hot' state) determine the VO_2 transition. Finally, dielectric functions of the 'cold' and 'hot' state are analyzed from the ellipsometric response of the film.

2.1. Raman Spectra

The raman spectra in **Figure 1** show how the V-to-O ratio is influenced by the oxygen flow from 1.4 to 2 sccm during deposition. The existence of around 20 available oxide compounds complicates the phase diagram of the vanadium/oxygen system.[20] Vanadium oxide phases with different stoichiometry can be deposited by carefully regulating the oxygen flow. This analysis proves that it is crucial to adequately control the oxygen quantity during deposition and annealing in order to achieve the appropriate composition, i.e., VO_2 instead of other oxides like V_2O_3, V_4O_7, or V_2O_5. For this reason a flow rate of 1.8 sccm was chosen for the thin films utilized in this paper, as it exhibits the desired VO_2 peaks.

2.2. Optical spectra

In order to highlight the thermochromic character, optical spectra in transmission and reflection are measured at 25 and at

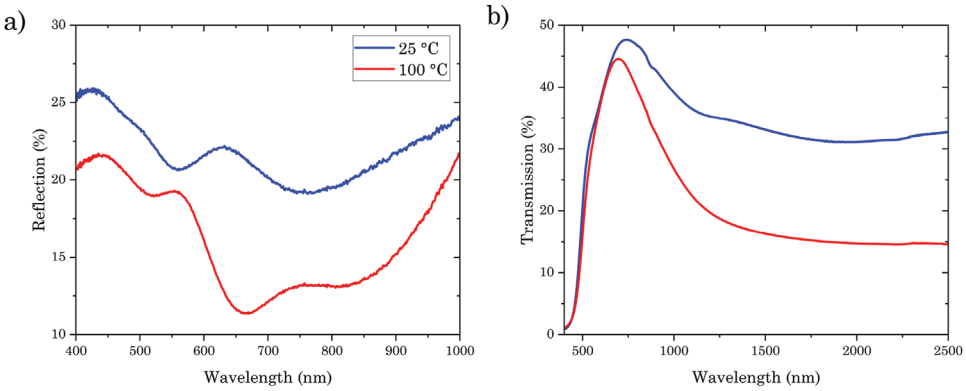

Figure 2. a) Reflection and b) transmission spectra at 25°C (blue) and 100°C (red) of a 200 nm VO_2 thin film. Reflection measurement are carried out using a Si substrate and transmission on a glass substrate.

100°C on a thin film deposited with the O_2 flow set to 1.8 sccm (**Figure 2**) and subsequently annealed as described in the experimental section. Upon heating, a maximum reflection contrast of 10 % (at 650 nm) and an approximate transmission contrast of 20 % (at 2500 nm) were observed. These findings highlight the significant changes in optical behavior associated with the transition from the monoclinic to the rutile phase of a VO_2 film.

Ellipsometry measurements were performed on the same sample with angles of incidence (AOI) of 50°, 55°, and 60°. The resulting 'cold' and 'hot' real and imaginary parts of the dielectric function are plotted in **Figure 3**. In the model fitting, a three-layer model composed of roughness layer/VO_2/glass with air as ambient material is applied to represent the sample. The surface roughness is mandatory because ellipsometry measurements are highly sensitive to the surface characteristics. This layer is modeled by a Maxwell-Garnett effective medium approximation with a mixture of VO_2 and air.

The best fit to the ellipsometric data was obtained when considering a film composed of two regions. The first one is fully

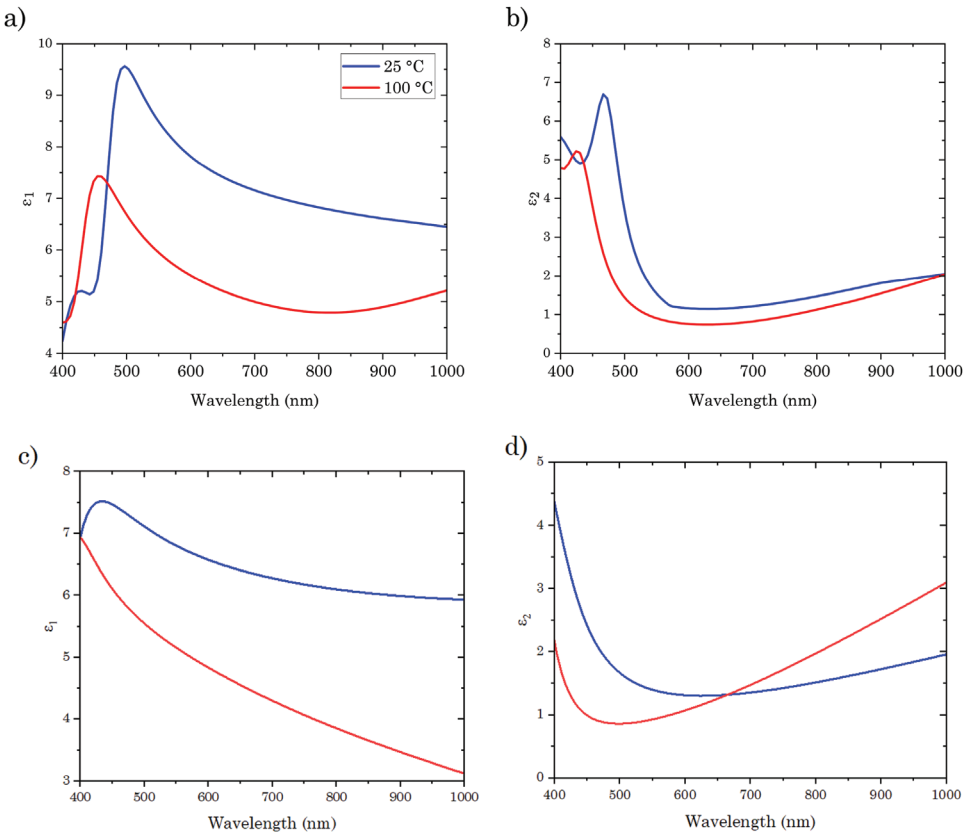

Figure 3. Dielectric function real part ϵ_1 and imaginary part ϵ_2 of VO_2 (a and b) and Au NPs-doped VO_2 (c and d) at 25°C (blue) and 100°C (red). Both samples on Si substrate.

Table 1. Lorentz fitting parameters for VO_2. The ϵ_∞ values are respectively equal to 4.3 ± 0.1 and 3.4 ± 0.6 for the 'cold' and 'hot' states, respectively.

Temperature		ω_j [eV]	S_j [eV^2]	γ_j [eV]
25°C	Lorentz 1	2.640 ± 0.008	3.667 ± 0.254	0.301 ± 0.024
	Lorentz 2	3.194 ± 0.015	14.317 ± 0.740	0.853 ± 0.039
100°C	Lorentz 1	2.886 ± 0.047	4.237 ± 3.034	0.410 ± 0.167
	Lorentz 2	1.266 ± 0.087	1.660 ± 1.277	0.840 ± 0.421
	Lorentz 3	3.384 ± 0.105	11.307 ± 10.228	0.602 ± 0.475

dense and characterized by a thickness of 168.8 ± 2.9 nm. On top of the dense region we added another layer that is 52 ± 0.5 nm thick and characterized by an air fraction equal to 35 ± 1 %. The measurement is done till a wavelength of 1000 nm and extrapolated up to 2500 nm. For the description of the VO_2 layer, Lorentzian oscillators are selected:

$$\epsilon(\omega) = \epsilon_\infty + \sum_j \frac{S_j}{\omega_j^2 - \omega^2 - i\gamma_j\omega} \tag{1}$$

where ω_j represents the resonant frequency, γ_j the damping factor and S_j the oscillator strength. **Table 1** displays the best fitting parameters for the Lorentz oscillators in the 'cold' and 'hot' states, respectively. An equivalent approach for modeling was proposed by Dai et al.[24] and Currie et al.[25] The fitting mean square errors (MSE) associated to the ellipsometry data are 4.1° in 'cold' state and 7.0° in 'hot' state, respectively, demonstrating a good agreement between model and data. The optical properties ϵ_1 and ϵ_2 represented here are employed for the simulations further on. An exception is done for simulations where the NPs are incorporated inside VO_2. In order to simulate a NPs/doped VO_2, another VO_2 refractive index has been measured for a sample coupled with NPs where an effective medium of Au and Air is used to model the NPs layer at the surface. The presence of this layer will modify the oscillator parameters of the VO_2 (see **Table 2**) and by consequence, the indices (Figure 3c,d). An important comment is that in the hot state, the real part ϵ_1 is never negative and so the behavior of the VO_2 is not really metallic but rather semiconducting. This is the result of our ellipsometric model where no Drude term, characterizing metallic behaviour, involved for the fitting.

Table 2. Lorentz fitting parameters for doped VO_2. The ϵ_∞ values are respectively equal to 4.2 ± 0.3 and 7.4 ± 0.1 for the 'cold' and 'hot' states, respectively.

Temperature		ω_j [eV]	S_j [eV^2]	γ_j [eV]
25°C	Lorentz 1	1.224 ± 0.049	0.448 ± 0.166	0.909 ± 0.378
	Lorentz 2	3.285 ± 0.074	30.542 ± 3.488	1.908 ± 0.166
100°C	Lorentz 1	3.025 ± 0.041	7.103 ± 2.214	0.581 ± 0.153
	Lorentz 2	1.069 ± 0.117	4.340 ± 1.967	0.638 ± 0.198
	Lorentz 3	4.396 ± 16.165	22.504 ± 10.228	0.388 ± 0.154

3. Nanoplasmonic Thermochromic Platforms

First, we analyze the NP coverage according to the APTMS solution dipping time, and then we study the plasmonic results for the VO_2/NP (particles on surface) and VO_2/NP/VO_2 (sandwich structure) platforms.

3.1. Grafting of Au NPs on the VO_2 Film

Let us first consider the optical properties of the Au NPs in solution. At the end of the synthesis the color of the colloidal solution becomes burgundy. The LSPR band of our Au solution is located at about 520 nm. According to the work of Haiss et al.,[26] the diameter of the nanoparticles d can be determined from the position of the resonance peak (λ_{SPR}) using

$$d = \frac{\ln\left(\frac{\lambda_{SPR}-\lambda_0}{L_1}\right)}{L_2} \tag{2}$$

where λ_0, L_1, and L_2 are experimental constants equal to 512 nm, 6.53 nm and 0.0216 nm^{-1}, coming from Haiss' work.[26] These authors have shown that for nanoparticle sizes larger than 25 nm both the theoretical and the experimental peak positions are precisely fitted by an exponential function (**Figure 5** in ref. [26]) resulting in Equation (2). Applying this equation to extinction spectra measured on our colloidal solution yields nanoparticle diameters close to 28 nm, in agreement to the values determined from the SEM analysis (presented further on).

The experimental protocol is composed of sequential immersion in APTMS and Au NP solution. The APTMS step plays a crucial role in anchoring amine linkers having a strong affinity for gold onto the VO_2 surface.[27] The linkers bind to the sample surface via the -OH groups and their methoxy function but, in order of maintaining the thermochromic behavior of the layer, no strong activation process (such as pirhana solution) can be used. The following results demonstrate the influence of immersion time on the surface coverage. Indeed, by measuring the absorption spectra of a VO_2 sample coated with Au NPs after two different immersion durations: 10h in APTMS followed by 6h in Au NPs solution, and 4h in APTMS followed by 2h in Au NPs solution (**Figure 4**), distinct absorption spectra are observed. The baseline of all these spectra is recorded on the VO_2 sample prior to anchoring of NPs. The signal is therefore entirely related to the plasmonic response.

In a first approximation, the extinction peak associated to the LSPR is controlled by three parameters: the peak intensity, the centre wavelength or energy and the full-width of the peak at half maximum (FWHM). The parameters can be related to the density of particles, their average size and their polydispersity, respectively. In solution at the end of the synthesis, only one peak is observed at about 520 nm, as pointed out earlier. In the case of 10h in APTMS (Figure 4, orange curve), the extinction spectrum is more complex. Two plasmonic peaks (broader than in solution) are observed at 530 nm and around 650 nm. The first one can be associated with the immobilization of isolated spherical NPs, while the second one indicates that NPs clusters are present on the surface alongside the isolated NPs. For the second protocol with shorter immersion duration (Figure 4, black curve), the

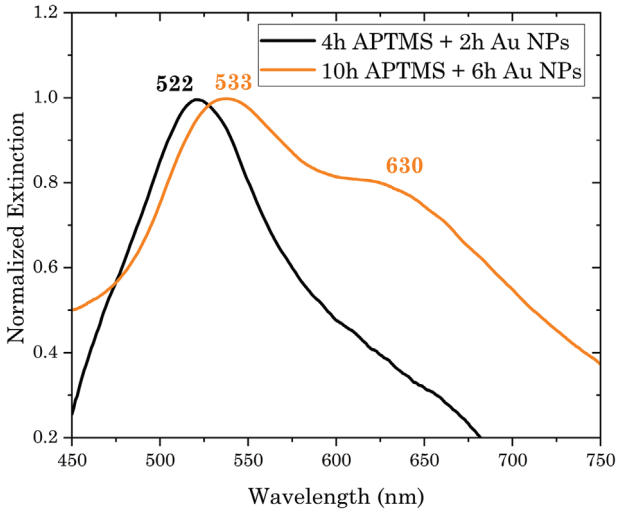

Figure 4. Normalized extinction spectra for VO_2 thin film on glass after two different Au NP grafting protocol durations.

cluster peak is not observed and only a single peak is visible, indicating that a monolayer of Au NPs is successfully grafted on VO_2.

By studying the effects of immersion times in APTMS and Au NPs solutions independently on plasmonic peaks, additional results (not shown in this paper) demonstrate that an increased immersion time in Au NP solution enhances the plasmonic peak visibility, but around 6h of immersion time an undesirable second plasmonic peak appears. Regarding the grafting of APTMS linker, longer immersion leads to peak disappearance due to organic layer formation.[28] The optimal grafting protocol is thus an immersion during 4h in the APTMS solution followed by dipping for 2h in the Au NP solution.

Consequently, this protocol is selected for the rest of the study. Additionally, a noticeable difference is observed in the λ_{LSPR} of the first peak between the two spectra. This phenomenon arises from the higher number of NPs present in the first condition (orange curve), where the isolated NPs are in close proximity and can interact with each other, resulting in a shift of the plasmonic resonance towards higher wavelengths.[29,30]

The representative SEM image in Figure 5 (left) provides further confirmation about the presence of numerous clusters after 10h in APTMS followed by 6h in Au NPs. The cluster sizes vary from 2 to 4 µm. The NPs have an average diameter of about 35 nm. The NPs are not truly isolated but rather grouped together, forming small clusters composed of dozens of NPs. In contrast, for the case of 4h in linker followed by 2h in NPs (Figure 5, right and **Figure 6**), a distinct monolayer is clearly apparent with an almost homogeneous distribution on the surface, resulting in a calculated coverage factor of approximately 13 %. Moreover, although some clusters are still present on the layer, no second plasmonic peak appears in the extinction spectra. This image helps to understand the first peak λ_{LSPR} difference between the two platforms produced thanks to the aforementioned protocols. Here, the NPs are most of the time well-isolated from each other and their size is estimated to be between 30–35 nm.

These measurements demonstrate the advantages of this grafting method. The coverage factor can be easily tuned by changing the immersion time. For exemple, **Figure 7** shows a top-view SEM of a VO_2 layer after 4h of dipping in APTMS solution and 30 min of Au NP solution. Here, the NP coverage factor is reduced to 2.4 % due to the shorter immersion time. Concerning, the size of NPs, it can also be tuned separately by varying the reaction time in the Turkevich method.

When NPs are coupled with thin films, these two factors are related if the NPs are synthesized by magnetron sputtering or pulsed laser deposition. In that case, the size and coverage simultaneously depend on the NP deposition time.[31,32]

3.2. Au NPs on VO_2 Surface

Now that the protocol to graft a NP monolayer onto a 200 nm thick VO_2 layer is established, the influence of the temperature, and so the VO_2 phase, can be investigated. To do this, extinction spectra are measured at 25 and 100°C, as shown in **Figure 8**. These spectra are normalized using a VO_2 sample without NPs as baseline, so the signal only represents the NP contribution. Here, the phase transition slightly influences the plasmonic peak resulting in a red-shift of approximately 12 nm. This behaviour can be attributed to the change in the NP environment, mediated by the temperature-dependent refractive index of VO_2. The plasmonic shift is relatively weak because there is a limited contact between VO_2 and Au NPs, as the NPs are just sitting on the film and are predominantly surrounded by ambient air, which is not influenced by the variation of temperature.

A strategy to enhance the plasmonic shift is to increase the Au NP-VO_2 contact by incorporating the NPs within the VO_2 matrix, creating a VO_2/NPs/VO_2 ('sandwich') platform, potentially leading to a larger modulation, as discussed next.

3.3. Au NPs Embedded in VO_2

We study a new platform composed of a second layer of VO_2 deposited above the NPs, while maintaining a total thickness of 200 nm, so the hybrid coating is made of two 100 nm layers (see SEM image in **Figure 9**). The corresponding extinction spectra in both VO_2 states are represented in **Figure 10**. We remark that the plasmonic shift is significantly improved and reaches around 23 nm. However, compared to the previous platform (NPs on VO_2 surface), an increase in temperature now leads to a blue-shift, so toward lower wavelengths.

The blue-shift agrees with a quasi-static electromagnetic analysis. In the quasi-static regime, a resonance occurs when the denominator of the polarizability α of a NP of relative permittivity ϵ_{NP} surrounded by a host medium ϵ_{VO_2} goes to zero, i.e., when $\epsilon_{NP} = -2\,\epsilon_{VO_2}$. This is also known as the Fröhlich condition.[33] In the case of VO_2, the dielectric function decreases as the material switches from the monoclinic phase (25°C) to the rutile phase (100°C) after 460 nm (see Figure 3a). Referring to the previous equation, a less negative ϵ_{NP} is required to induce a LSPR in the monoclinic ('cold') phase as compared to the rutile ('hot') phase. Given that the ϵ_{NP} value of gold gradually decreases toward more negative values with increasing wavelength,[34] a corresponding

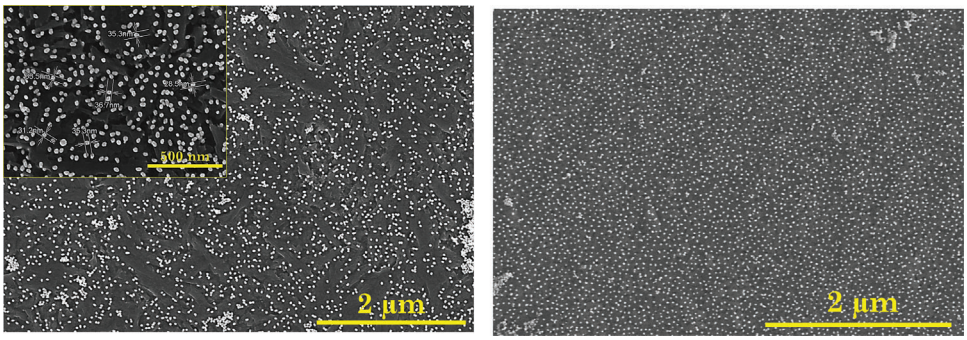

Figure 5. SEM images on VO_2 on Si substrate after 10h in APTMS + 6h in NP solution (left) and after 4h in APTMS + 2h in NP solution (right). An inset is present with a higher magnification to distinguish the NPs' size.

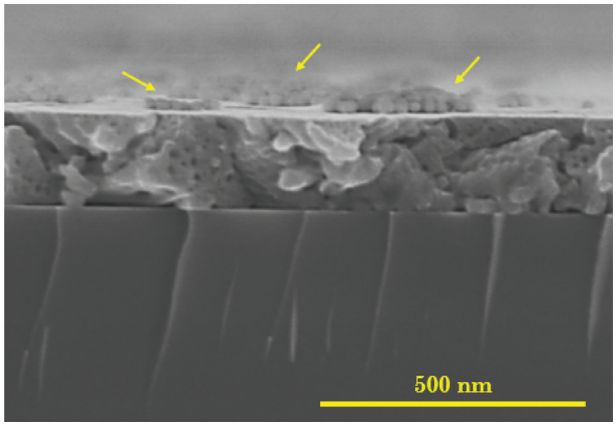

Figure 6. SEM image of 200 nm NPs/VO_2. Yellow arrows correspond to Au NPs. The substrate is silicon.

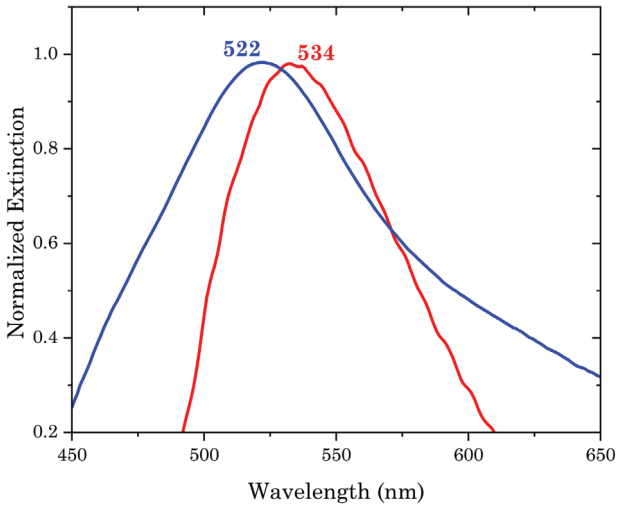

Figure 8. Normalized extinction spectra for 200 nm VO_2 coupled with a monolayer of Au NPs on top of VO_2 film surface at 25°C (blue line) and 100°C (red line).

blue-shift becomes evident with increasing temperature. Thus, in the 'hot' state, the quasi-static Fröhlich condition is respected at a lower wavelength compared to the 'cold' state. Identical negative shifts were measured in similar studies.[31,32,35,36]

Note that for the first experimental platform, i.e., when the gold NPs sit on the VO_2 surface, one cannot directly apply Fröhlich's equation which requires the NPs to be fully embedded in a homogeneous matrix. We therefore consider this situation (and subsequent ones) from a numerical point of view.

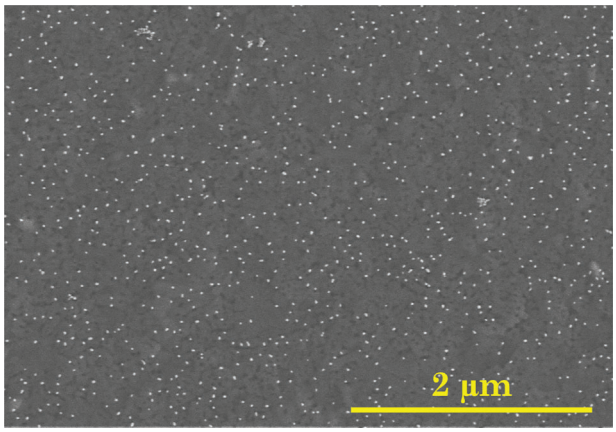

Figure 7. SEM top-view of a VO_2 200 nm thin film after a grafting protocol composed of 4h of APTMS and 30 min of Au NPs.

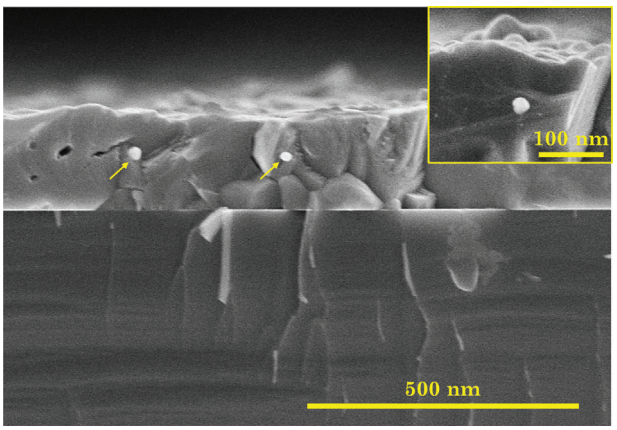

Figure 9. SEM image of 200 nm VO_2/NPs/VO_2. Bright spots indicated with yellow arrows correspond to Au NPs. The substrate is silicon.

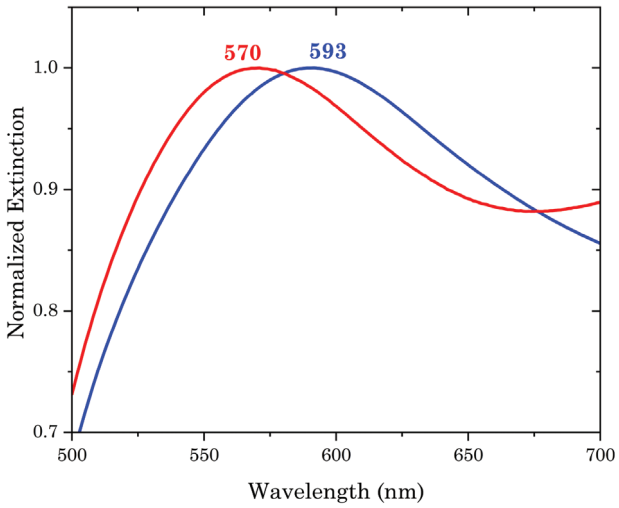

Figure 10. Normalized extinction spectra for 200 nm VO_2/NPs/VO_2 on glass at 25°C (blue line) and 100°C (red line).

4. Modeling NPs with a VO_2 Thin Film

The two experimental structures (NPs on the VO_2 surface and NPs inside VO_2) can be viewed as two specific situations of an interesting structural sequence. Using numerical modeling with COMSOL Multiphysics, we can examine the entire sequence, as depicted in **Figure 11**. By introducing a single parameter d, which quantifies the distance between the VO_2 planar surface and the bottom of the 30 nm Au NPs, we can explore the progression from (a) NPs fully integrated inside the VO_2 to (b) NPs encased in a thin VO_2 shell partially inserted into the VO_2, to (c) NPs on the VO_2 surface, and finally, to (d) NPs in air near the surface. Furthermore, periodic boundary conditions are applied in the horizontal surface directions with a period of 100 nm (i.e., more than three times the NP diameter). We assume spherical particles, so the simulations are 3D, with a 2D square lattice in the plane, and perpendicular incidence from the top.

Note that only for d between -35 to -1 nm we employ a VO_2 shell (see Figure 11b), with thickness equal to $|d|$. We do not use the shell for d values below -36 nm (see Figure 11a), to prevent the formation of an excessively large and nonphysical shell. The NP covered with a VO_2 shell is made to represent the deposition of a thin layer via magnetron sputtering on top of the NPs. In this process, sputtered atoms would diffuse to conform to the shape of the NPs. After a more substantial deposition duration, the shell gradually becomes dominant, leading to a coalescence and the formation of a flat layer, as illustrated in configuration Figure 11a. In any case, the results become insensitive to the overlayer thickness around $d = -40$ nm. Despite the fact that in experiments, the NPs were incorporated until a distance d of -100 nm, the simulations were stopped at -65 nm as no variation appeared after this point. Concerning the refractive indices used, the doped VO_2 is employed for $d < 0$ and the non-doped VO_2 for $d \geqslant 0$. Both refractive indices are presented in Figure 3.

First, we study the plasmonic peak position relative to the parameter d (**Figure 12**). For $d > 0$ (Figure 11d), the NP surrounding medium is air, without direct contact with VO_2. In this configuration, VO_2 exerts no influence on the plasmonic effect, and the peak position is solely determined by the Fröhlich condition between only one NP and air, resulting in a peak at approximately 510 nm (see $d = 50$ nm). When d is reduced, the NPs approach and begin to interact with the VO_2 surface, leading to a separation of the two VO_2 states (see e.g., around $d = 10$ nm). This interaction leads to a slight shift of approximately 10 nm between the 'hot' and 'cold' states, with the 'hot' state leading to a larger resonance wavelength than the 'cold' state. For a more detailed visualization, see **Figure 13**, where we plot the difference (called 'plasmonic shift') between the 'hot' and 'cold' peak points in Figure 12.

Similar trends are observed in our experimental results. Indeed, NPs sitting on the VO_2 surface (Figure 8) give a positive shift of around 12 nm, comparable to the 10 nm shift observed in simulations (at $d = 0$). The peak positions are also similar with a 522 nm ('cold') and 534 nm ('hot') for experiments, while the calculated values are 507 nm ('cold') and 517 nm ('hot').

When the NPs are very slightly submerged at $d = -2$ nm, a pronounced shift of around -10 nm is observed. In this configuration, in addition to the subtle indentation of the NP (Figure 11b), there is now a 2 nm-thick VO_2 shell surrounding the NP. As depicted in Figure 12, this minor alteration has a very drastic and substantial impact on the results. With just a 2 nm-thick shell, the plasmonic peaks move towards higher wavelengths, resulting in a negative shift of -10 nm (negative because the 'hot' peak position drops below the 'cold' one). As the NPs penetrate deeper and the shell grows, the plasmonic bands continue to move toward infrared wavelengths, reaching 600 and 660 nm, with the shift increasing to -60 nm.

When d goes below about -50 nm (Figure 11a), the peak position stabilizes, forming a plateau corresponding to a shift around -60 nm. All these results demonstrate the VO_2 influence, with more encapsulation leading to strong plasmonic shifts toward the infrared. This effect can be understood as the effective dielectric constant around the NP (ϵ_{medium}) changes from air to VO_2, the Fröhlich condition ($\epsilon_{NP} = -2\epsilon_{medium}$) is satisfied for longer wavelengths, as ϵ_{NP} is more negative at this range.

When NPs are inside VO_2, the experiments (Figure 10) show a shift around -23 nm, compared to the simulation result highlighting a bigger shift of about -60 nm. The disparities between experiments and simulations primarily come from the challenges in measuring the refractive index of VO_2, leading to a Mean Square Error indicating an approximate optical model for fitting. Consequently, minor variations in the experimental refractive indices can impact the results related to the plasmonic properties. As previously discussed, the surrounding refractive index of NPs has a substantial influence on plasmonic peak positions. In addition, other elements differ from the simulations, such as the NP disorder, the VO_2 roughness, and the Au refractive index. We note that the simulations are fairly insensitive to the precise period employed, except when going to very close, nearly-touching particles.

Finally, three distinct embedding conditions (with d = -40, -5, and 0 nm) were selected to illustrate the absorption spectra (**Figure 14**) and electric field profiles (**Figure 15**). As described earlier, a strong red-shift appears for the peaks when going from $d = 0$ nm to -5 nm (Figure 14c, b). In the context of electric fields, the classical dipolar resonance plasmonic behavior is present for d = 0 nm and -40 nm (Figure 15a,c). However, when d = -5 nm, the presence of the shell and the substrate complicates the

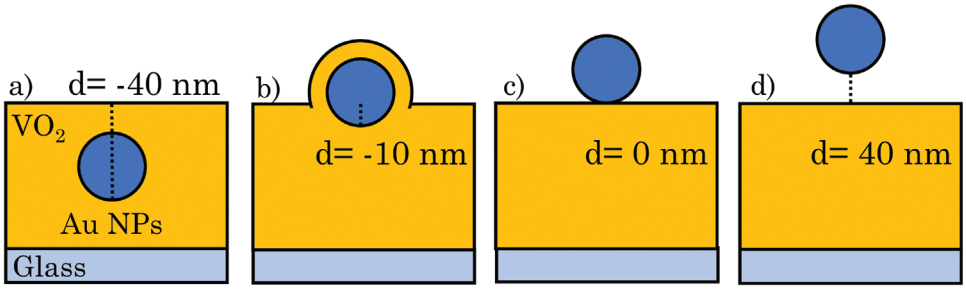

Figure 11. Visualization of four distinct configurations of Au NPs coupled with VO_2 with a) $d = -40$ nm, b) $d = -10$ nm (the shell thickness corresponds to $|d|$), c) $d = 0$ nm and d) $d = 40$ nm. The square unit cell period in the two planar directions is 100 nm.

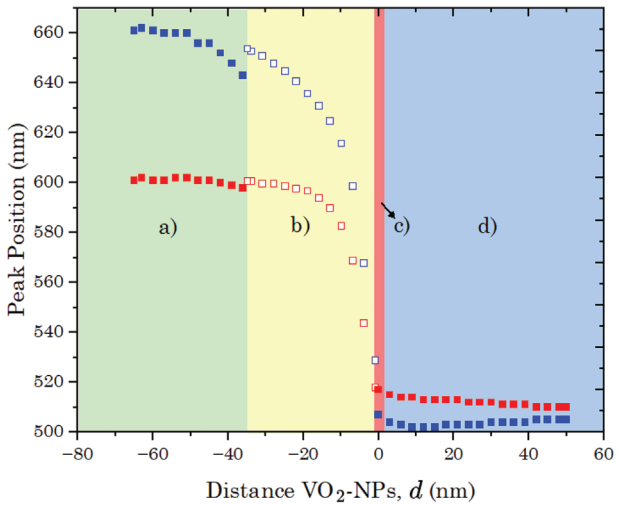

Figure 12. Plasmonic peak position in the 'cold' (blue) and 'hot' (red) state according to the separation distance d between VO_2 surface and NPs. Filled and empty squares represent calculations without and with a VO_2 shell, respectively. Colors and letters refer to the respective schematics in Figure 11. Doped VO_2 indices are used for $d<0$.

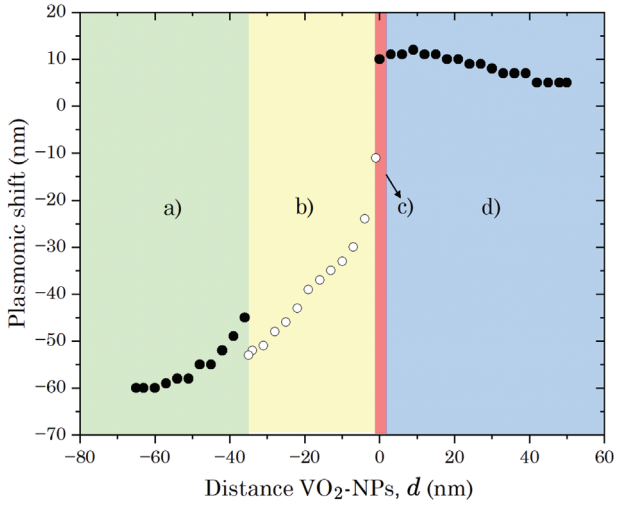

Figure 13. Difference between plasmonic peak position in the 'hot' and 'cold' state, called plasmonic shift, according to the separation distance d. Colors and letters refer to the respective schematics in Figure 11. Doped VO_2 indices are used for $d<0$.

electric field pattern: the dipole-like field is pulled downward toward the VO_2 layer, and there is localization in the VO_2 shell, leading to the drastic shift present in Figure 13.

Another point is the higher absorption (Figure 14, compare c with a,b) and field intensity (Figure 15, compare c with a,b) when the NP is surrounded by VO_2 compared to air around. This can be understood via the quasistatic polarizability, which is proportional to $|(\epsilon_{NP} - \tilde{}\epsilon_{medium})/(\epsilon_{NP} + 2\tilde{}\epsilon_{medium})|$. The latter is about ten times larger when the medium is VO_2 around the Au NP (Figures 14c and 15c) than when it is air (Figures 14a and 15a).

Finally, in Figure 15b the electric field magnitude tends to be higher just on the outside of the VO_2 shell-air interface, compared to just inside. This can be explained via the perpendicular boundary condition: $\epsilon_{VO_2} E_{p,VO_2} = \epsilon_{air} E_{p,air}$, with E_p the perpendicular component of the electrical field inside the respective material. As ϵ_{VO_2} is larger than ϵ_{air}, E_{p,VO_2} decreases compared to $E_{p,air}$.

5. Conclusion

We investigated the coupling between VO_2 and metal nanoparticles (NPs) both experimentally and numerically. Using low-pressure plasma-based reactive DC magnetron sputtering, we successfully deposited VO_2 thin films, which exhibited significant changes in optical behavior during the transition from the monoclinic to the rutile phase. After that, we grafted gold NPs onto the VO_2 surface via sequential immersion in APTMS and Au NP solutions, finding that immersion time significantly affected the absorption spectra. Shorter immersion times resulted in a monolayer of well-isolated Au NPs, allowing independent adjustment of NP size and surface coverage.

The temperature influence on plasmonic resonance was studied for monolayer (NPs/VO_2) and bilayer ($VO_2/NPs/VO_2$) geometries. A small shift of +12 nm was observed for surface particles, while encapsulating Au NPs within the VO_2 matrix resulted in a -23 nm shift. Via numerical analysis, we linked the experiments and extended the range of geometries of our hybrid materials under study. The results demonstrated the tunability of the plasmonic shift by varying the NP position on the VO_2 layer, with the sandwich platform showing a broader range of plasmonic shifts compared to the platform made of NPs sitting on the film surface.

Overall, this research provides valuable insights into VO_2 thin film deposition and plasmonic property modulation through NP integration, with potential applications in smart windows, optical sensors, and optoelectronic devices.

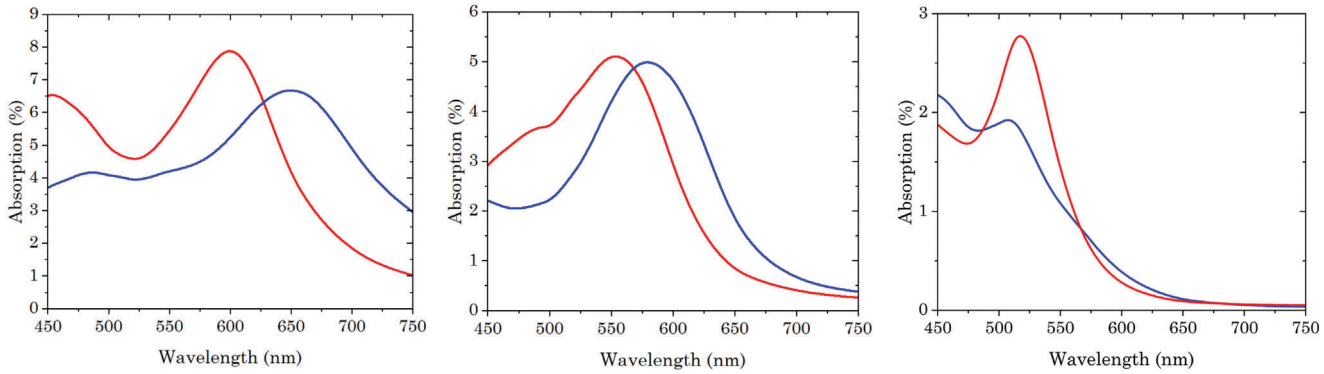

Figure 14. Simulated absorption spectra for d = -40 nm (left), d = -5 nm (center) and d = 0 nm (right) at 25°C (blue) and 100°C (red).

6. Experimental Section

This section introduces the employed technical methods and experimental parameters concerning the magnetron sputtering deposition and the (3-aminopropyl)trimethoxysilane (APTMS) grafting. Subsequently, the various tools to characterize or to simulate the VO_2 thin film are discussed.

Film Synthesis: Thin films of VO_2 were deposited in a stainless steel chamber utilizing a low-pressure plasma-based reactive DC magnetron sputtering method. A vanadium target with a diameter of 5 cm and a thickness of 0.6 cm (99.99 % purity) was employed. To produce the vanadium oxide layer a combination of argon and oxygen was introduced into the chamber at a constant working pressure of 1 mTorr (0.13 Pa) and a constant discharge current value of 0.3 A. The turbo-molecular pump backed by a dry pump achieved a residual pressure of 10^{-7} mTorr to guarantee good control over the film chemical composition. The substrate consisted of (100) single crystal silicon wafers or microscope glass slide fragments, washed with a aqueous detergent solution (3 % v/v RBS in water, Chemical Products R. Borghgraef S.A.). The use of any substrate depends on the characterization done. For example, a silicon substrate was preferred for Raman, reflection, ellipsometry, and SEM measurements. The glass substrate was employed, on the other hand, for transmission and absorption. However, previous research[37] showed only marginal variations in refractive indices between silicon and glass substrates, suggesting that substrate differences had little influence on results. The substrate was intentionally not heated and carried out at room temperature. During the film deposition process, the flux of argon and oxygen was fixed at 8 and 1.6 sccm (Standard cubic centimeters per minute), respectively. A deposition rate around 22 $nmmin^{-1}$ was obtained with this configuration and the thin film thickness was about 200 nm. After that, the sample was annealed for 120 min at 500 °C in pure oxygen atmosphere (about 3 Torr), in the same chamber, to obtain the desired VO_2 monoclinic phase. Another procedure must be utilized in order to obtain the second platform, VO_2/NP/VO_2. First, a 100 nm thick layer of VO_x with exactly the same deposition parameters as those on the last platform was deposited. The only difference was that the annealing was not yet performed. Afterwards, the Au NPs was grafted without changing the protocol described in the next section. Finally, the second layer of 100 nm VO_x was deposited on the top of Au NPs, and the whole sample was then annealed using the same conditions as for NP/VO_2.

NP Synthesis and APTMS Functionalization: To synthesize Au NPs with a diameter of approximately 30–40 nm, a slightly modified Turkevich approach was employed. This involved the chemical reduction of gold(III) chloride trihydrate using sodium citrate in a boiling aqueous solution.[38] Specifically, $HAuCl_4$ (99 ml, 0.0025 M) solution was heated to the boiling point, and then sodium citrate (1 ml, 0.0388 M) solution was added. Continuous agitation of the liquid was done using a Teflon-coated magnetic bar. The reddish solution containing Au NPs was cooled to room temperature after 15 min. All aqueous solutions were prepared with ultra-pure water of resistivity greater than 18 MΩcm. For functionalization, the surface of VO_2 thin films was first cleaned and activated prior to grafting the organic linkers by immersing samples in a 3 % solution of RBS, acetone, and methanol in an ultrasonic bath for 30, 10, and 10 min, respectively. A 5 % (v/v) solution of APTMS in methanol was used to prepare the linker solution. Clean VO_2 thin films were then dipped in the linker solution for the required duration. To finish, the functionalized VO_2 is dipped in the Au NP solution and then rinced with water to remove any excess of unbound NPs. These activation and grafting procedures maintain the thermochromic behavior of the VO_2 films, as shown in the next paragraphs.

Film Characterization Tools: Reflectivity measurements were performed using a custom-made reflectometer that uses a CCS200 CCD spectrometer in combination with a RP20 bifurcated fiber and a SLS201L tungsten-halogen light source (Thorlabs, France). The reflectometer spectral range is from 380 to 1000 nm and the reflectometer was operated at normal incidence. The refractive indices, n and k, of as-produced VO_2 films were measured using spectroscopic ellipsometry using an Accurion EP3-SE nulling spectroscopic ellipsometer in the PCSA

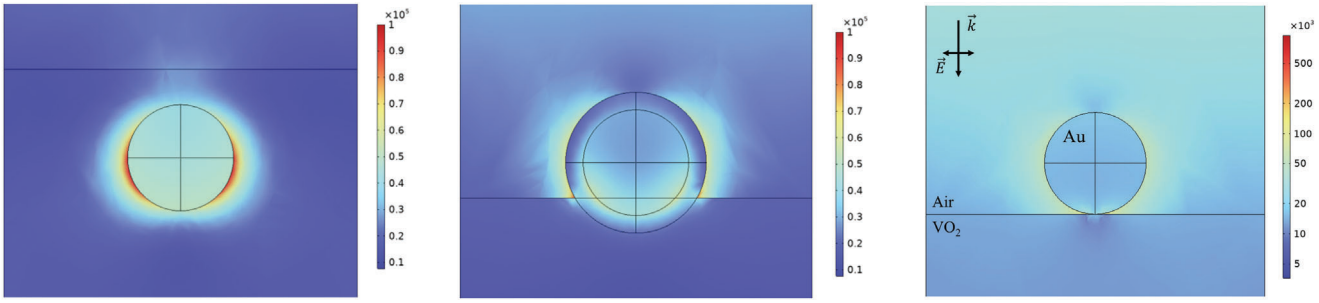

Figure 15. Simulated electric field (absolute value) around a 30 nm NP with cold VO_2 at the peak wavelength for d = -40 nm (left), d = -5 nm (center) and d = 0 nm (right).

(polarizer-compensator-sample-analyzer) configuration, covering a spectral range from 400 to 900 nm. The angle of incidence (AOI) was set to 50°, 55°, and 60° for the ellipsometric analysis. Transmission spectra were obtained using a Cary 5000 UV–Vis–NIR spectrometer ranging from 200 to 2500 nm. Temperature control during the measurements was maintained with a THMS600 Linkam heating/cooling stage. Since the study involved nanometer-scale thin film coatings, the crystalline composition was determined through Raman spectroscopy carried out in a Bruker Senterra spectrometer equipped with a CCD detector and a HeNe laser (532 nm) at 20 mW. NP images were obtained using a field emission gun scanning electron microscope (FEG-SEM Hitachi SU8020) with a 5 kV acceleration voltage. The NP coverage calculations were based on the thresholding tool using the ImageJ software.[39] Concerning the absorption spectra, they were all measured using a Genesys 10S UV-visible spectrophotometer (Thermo Fisher Scientifc). The sample was illuminated by a xenon flash lamp, and a silicon photodiode detector provides the transmittance measurement. Because of the monochromator and light source, the spectral range was 190 to 1100 nm. For analysis of plasmonic resonance of Au NPs coupled with VO_2, the baseline was composed of a bare VO_2 thin film without NPs.

Simulation Tool: For the gold NPs with VO_2, COMSOL Multiphysics was utilized to simulate electromagnetic fields and compute absorption spectra. A 2D square lattice of gold NPs was considered. To achieve this, Floquet periodic boundary conditions was incorporated on the left and right sides of the modeling domain. The inter-particle distance was determined using a custom Python script for image analysis and nearest neighbor calculation, applied to the SEM images. The Port boundary condition at the top launches a plane wave at normal incidence and computes the reflected light, while the one at the bottom calculated the transmitted light. Absorption due to the nanoparticles involved integrating electromagnetic losses over the volume of the nanoparticles. The elementary shape function utilized to approximate the electric field within each tetrahedral meshing element was quadratic. In accordance with this selection, five mesh elements were employed per wavelength as recommended in the COMSOL documentation. The optical constants for gold were extracted from the experimental data of Johnson and Christy,[34] with considerations for NP size corrections. The refractive indices of VO_2 were determined through ellipsometry as mentioned before, and will be presented in Section 2.2.

Acknowledgements

S. K. is Research Director of the National Funds for Scientific Research (FRS-FNRS Belgium). G. S. acknowledged the FRS-FNRS for financial support (FRIA grant). C. R., G. R., and B. M. acknowledged support from the Action de Recherche Concertée (project ARC-23/27 UMONS3).

Conflict of Interest

The authors declare no conflict of interest.

Data Availability Statement

The data that support the findings of this study are available from the corresponding author upon reasonable request.

Keywords

gold, metal nanoparticles, optical simulation, thermochromic material, VO_2

Received: February 27, 2024
Revised: June 15, 2024
Published online:

[1] F. J. Morin, *Phys. Rev. Lett.* **1959**, *3*, 34.
[2] G. Savorianakis, K. Mita, T. Shimizu, S. Konstantinidis, M. Voué, B. Maes, *J. Appl. Phys.* **2021**, *129*, 185306.
[3] M. A. Kats, D. Sharma, J. Lin, P. Genevet, R. Blanchard, Z. Yang, M. M. Qazilbash, D. N. Basov, S. Ramanathan, F. Capasso, *Appl. Phys. Lett.* **2012**, *101*, 221101.
[4] Y. Cui, Y. Ke, C. Liu, Z. Chen, N. Wang, L. Zhang, Y. Zhou, S. Wang, Y. Gao, Y. Long, *Joule* **2018**, *2*, 1707.
[5] B. Li, S. Tian, L. Zhou, S. Wu, T. Ma, G. He, B. Liu, X. Zhao, *Adv. Opt. Mater.* **2023**, *12*, 2302042.
[6] B.-G. Chae, H.-T. Kim, S.-J. Yun, B.-J. Kim, Y.-W. Lee, D.-H. Youn, K.-Y. Kang, *Electrochem. Solid-State Lett.* **2005**, *9*, C12.
[7] D. K. Manousou, S. Gardelis, M. Calamiotou, E. Syskakis, *Mater. Lett.* **2021**, *299*, 130086.
[8] E.-K. Koussi, F. Bourquard, T. Tite, D. Jamon, F. Garrelie, Y. Jourlin, *Appl. Surf. Sci.* **2020**, *521*, 146267.
[9] F. Dumas-Bouchiat, C. Champeaux, A. Catherinot, A. Crunteanu, P. Blondy, *Appl. Phys. Lett.* **2007**, *91*, 223505.
[10] R. Marvel, R. Harl, V. Craciun, B. Rogers, R. Haglund, *Acta Materialia* **2015**, *91*, 217.
[11] F. Wang, H. Chen, D. Lan, F. Zhang, Y. Sun, X. Zhang, S. Li, T. Cheng, *Adv. Opt. Mater.* **2021**, *9*, 2100795.
[12] T. Moot, C. Palin, S. Mitran, J. F. Cahoon, R. Lopez, *Adv. Opt. Mater.* **2016**, *4*, 578.
[13] D. O. Shin, J.-R. Jeong, T. H. Han, C. M. Koo, H.-J. Park, Y. T. Lim, S. O. Kim, *J. Mater. Chem.* **2010**, *20*, 7241.
[14] S. Gottam, C.-T. Tsai, L.-W. Wang, C.-T. Wang, C.-C. Lin, S.-Y. Chu, *Appl. Surf. Sci.* **2019**, *506*, 144981.
[15] J. Liang, L. Yu, Y. Wang, T. Xue, D. Lei, Z. Wang, X. Li, *Adv. Opt. Mater.* **2022**, *10*, 2102615.
[16] K. Kelly, E. Coronado, L. Zhao, G. Schatz, *J. Phys. Chem. B* **2003**, *107*, 668.
[17] G. Xu, Y. Chen, M. Tazawa, P. Jin, *J. Phys. Chem. B* **2006**, *110*, 2051.
[18] J. Orlianges, J. Leroy, A. Crunteanu, R. Mayet, P. Carles, *Appl. Phys. Lett.* **2012**, *101*, 133102.
[19] M. Sypabekova, A. Hagemann, D. Rho, S. Kim, *Biosensors* **2023**, *13*, 36.
[20] P. Hu, P. Hu, T. D. Vu, L. Ming, S. Wang, Y. Ke, X. Zeng, L. Mai, *Chem. Rev.* **2023**, *123*, 4353.
[21] C. Zhang, Q. Yang, C. Koughia, F. Ye, M. Sanayei, S.-J. Wen, S. Kasap, *Thin Solid Films* **2016**, *620*, 64.
[22] J. Huotari, J. Lappalainen, J. Eriksson, R. Bjorklund, E. Heinonen, I. Miinalainen, J. Puustinen, A. Lloyd Spetz, *J. Alloys Compd.* **2016**, *675*, 433.
[23] R. Hadjean, J.-P. Pereira-Ramos, C. Navone, M. Smirnov, *Chem. Mater.* **2008**, *20*, 1916.
[24] K. Dai, J. Lian, M. Miller, J. Wang, Y. Shi, Y. Liu, H. Song, X. Wang, *Opt. Mater. Express* **2019**, *9*, 663.
[25] M. Currie, M. A. Mastro, V. D. Wheeler, *Opt. Mater. Express* **2017**, *7*, 1697.
[26] W. Haiss, N. T. K. Thanh, J. Aveyard, D. G. Fernig, *Anal. Chem.* **2007**, *79*, 4215.
[27] D. F. S. Petri, G. Wenz, , P. Schunk, T. Schimmel, *Langmuir* **1999**, *15*, 4520.
[28] J. Howarter, J. Youngblood, *ACS J. Surf. Colloids* **2007**, *22*, 11142.
[29] G. A. Kelesidis, D. Gao, F. Starsich, S. Pratsinis, *Anal. Chem.* **2022**, *94*, 5310.
[30] H. Wang, *Sci. Rep.* **2018**, *8*, 9589.
[31] H. Zhou, X. Cao, M. Jiang, S. Bao, P. Jin, *Laser Photonics Rev.* **2014**, *8*, 617.
[32] A. K. Agrawal, A. Das, N. Gupta, K. Kumar, A. Dhawan, *Adv. Photonics Res.* **2022**, *3*, 2100253.

[33] O. Schnitzer, V. Giannini, S. Maier, R. Craster, *Proc. R. Soc. A* **2016**, *472*, 20160258.
[34] P. B. Johnson, R. W. Christy, *Phys. Rev. B* **1972**, *6*, 4370.
[35] J. Liang, X. Song, P. Li, L. Zhou, J. Guo, *Mater. Res. Express* **2019**, *6*, 0850f6.
[36] J. Liang, L. Yu, Y. Wang, T. Xue, D. Lei, Z. Wang, X. Li, *Adv. Opt. Mater.* **2022**, *10*, 2102615.
[37] C. Wan, Z. Zhang, D. Woolf, C. M. Hessel, J. Rensberg, J. M. Hensley, Y. Xiao, A. Shahsafi, J. Salman, S. Richter, Y. Sun, M. M. Qazilbash, R. Schmidt-Grund, C. Ronning, S. Ramanathan, M. A. Kats, *Ann. Phys.*, *531*, 1900188.
[38] J. Kimling, M. Maier, B. Okenve, V. Kotaidis, H. Ballot, A. Plech, *J. Phys. Chem. B* **2006**, *110*, 15700.
[39] C. Schneider, W. Rasband, K. Eliceiri, *Nat. Methods* **2012**, *9*, 671.